Quantitative live-cell imaging and 3D modeling reveal critical functional features in the cytosolic complex of phagocyte NADPH oxidase

Received for publication, November 29, 2018, and in revised form, January 8, 2019 Published, Papers in Press, January 10, 2019, DOI 10.1074/jbc.RA118.006864

Cornelia S. Ziegler[‡1], Leïla Bouchab[‡2], Marc Tramier[§], Dominique Durand[¶], Franck Fieschi[‖], Sophie Dupré-Crochet[‡], Fabienne Mérola[‡], Oliver Nüße[‡3], and Marie Erard[‡4]

From the [‡]Laboratoire de Chimie Physique, CNRS, Université Paris-Sud, Université Paris-Saclay, 91405, Orsay France, the [§]Université Rennes, CNRS, Institut de Génétique et Développement de Rennes – UMR 6290, BIOSIT – UMS 3480, F-35000 Rennes, France, the [¶]Institute for Integrative Biology of the Cell, CEA, CNRS UMR 9198, Université Paris-Sud, Université Paris-Saclay, 91190 Gif-sur-Yvette, France, and the [‖]Université Grenoble Alpes, CNRS, CEA, Institut de Biologie Structurale, F-38044 Grenoble, France

Edited by Wolfgang Peti

Phagocyte NADPH oxidase produces superoxide anions, a precursor of reactive oxygen species (ROS) critical for host responses to microbial infections. However, uncontrolled ROS production contributes to inflammation, making NADPH oxidase a major drug target. It consists of two membranous (Nox2 and p22^{phox}) and three cytosolic subunits (p40^{phox}, p47^{phox}, and p67^{phox}) that undergo structural changes during enzyme activation. Unraveling the interactions between these subunits and the resulting conformation of the complex could shed light on NADPH oxidase regulation and help identify inhibition sites. However, the structures and the interactions of flexible proteins comprising several well-structured domains connected by intrinsically disordered protein segments are difficult to investigate by conventional techniques such as X-ray crystallography, NMR, or cryo-EM. Here, we developed an analytical strategy based on FRET–fluorescence lifetime imaging (FLIM) and fluorescence cross-correlation spectroscopy (FCCS) to structurally and quantitatively characterize NADPH oxidase in live cells. We characterized the inter- and intramolecular interactions of its cytosolic subunits by elucidating their conformation, stoichiometry, interacting fraction, and affinities in live cells. Our results revealed that the three subunits have a 1:1:1 stoichiometry and that nearly 100% of them are present in complexes in living cells. Furthermore, combining FRET data with small-angle X-ray scattering (SAXS) models and published crystal structures of isolated domains and subunits, we built a 3D model of the entire cytosolic complex. The model disclosed an elongated complex containing a flexible hinge separating two domains ideally positioned at one end of the complex and critical for oxidase activation and interactions with membrane components.

Numerous proteins contain intrinsically disordered regions (1, 2). Their growing number challenges the paradigm of a strong relationship between structure and function. Those proteins require new strategies to study their shape and their interactions. Here we focus on proteins composed of structured domains linked by disordered segments. Those segments and thus the whole protein can adopt a broad ensemble of conformations. These ensembles are highly influenced by their environment. In particular, the molecular crowding, the local ion concentrations, pH, or viscosity present in live cells may change the set of accessible conformations. Nevertheless, when they are associated with diseases, knowledge about both their structure and their affinity with partners is essential to identify potential drug targets in medicinal chemistry. Their structural analysis calls for new *in situ* analytical strategies (1, 2). Here, we combined live cell FRET–FLIM[5] and FCCS approaches to propose an integrated analytical workflow for structural and quantitative studies of a protein complex composed of such multidomain proteins in their native environment. We applied this workflow to the intra- and intermolecular interactions of the cytosolic factors of the phagocyte NADPH oxidase complex.

The phagocyte NADPH oxidase is one of the seven isoforms of the Nox family and a major enzyme of the immune system because of its pronounced production of microbicidal reactive oxygen species (ROS). A pathological hyperactivity of this oxidase leads to chronic inflammation, which is associated with cardiovascular diseases, stroke, and chronic obstructive pulmonary disease (3). The activity is regulated by the spatiotemporal organization of the intra- and intermolecular interactions of its cytosolic subunits, p40^{phox}, p47^{phox}, and p67^{phox}, forming a soluble complex before activation. Upon activation, these subunits

This work was supported by "The Foundation for Medical Research Grant DCM20121225747," by LabExPALMGrant ANR-10-LABX-0039-PALM, and by the IDEX Paris Saclay (IRS BioProbe). The authors declare that they have no conflicts of interest with the contents of this article.

This article contains supporting text, Tables S1–S4, and Figs. S1–S12.

SAXS data have been released on the SASBDB under codes SASDEJ3, SASDEK3, and SASDEL3.

[1] Supported by a doctoral grant from IDEX Paris-Saclay.
[2] Supported by a doctoral grant from Region Île-de-France (DIM Malinf).

[3] To whom correspondence may be addressed. E-mail: oliver.nusse@u-psud.fr.
[4] To whom correspondence may be addressed. E-mail: marie.erard@u-psud.fr.

[5] The abbreviations used are: FLIM, fluorescence lifetime imaging; FCS, fluorescence correlation spectroscopy; FCCS, fluorescence cross-correlation spectroscopy; ROS, reactive oxygen species; SAXS, small-angle X-ray scattering; FP, fluorescent protein; CFP, cyan FP; YFP, yellow FP; RFP, red FP; PMA, phorbol myristate acetate; DPI, diphenyleneiodonium; TCSPC, time-correlated single photon counting.

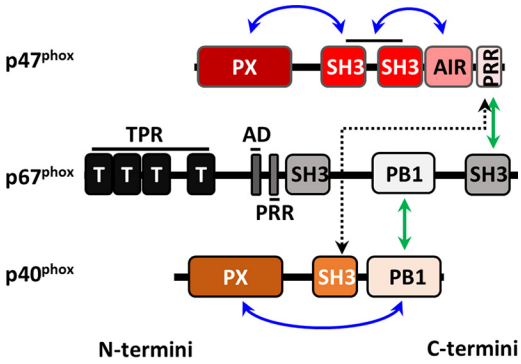

Figure 1. Structural organization of the NADPH oxidase. The domain structure of the three cytosolic subunits of the phagocyte NADPH oxidase in the resting state is shown. The domains and their positions in the proteins are drawn approximately to size. *Arrows* denote known intramolecular interactions (*blue*) and intermolecular interactions (*green*). The *dotted black line* represents the possible interaction between $p40^{phox}$ and $p47^{phox}$.

translocate together with the small GTPase Rac to the membrane subunits Nox2 and $p22^{phox}$ to form the active oxidase complex. The protein interactions within the cytosolic complex were extensively studied *in vitro* (Fig. 1) (3). In addition to the interactions between $p40^{phox}$ and $p67^{phox}$ or $p47^{phox}$ and $p67^{phox}$, an interaction between the SH3 domain of $p40^{phox}$ and the PRR domain of $p47^{phox}$ has been observed, but its physiological relevance is not clear (4). The structure of $p40^{phox}$ was entirely solved (5). The presence of intrinsically disordered regions in $p47^{phox}$ and $p67^{phox}$, predicted from their sequence (6), prevented the crystallization of the whole subunits. Only domains either isolated or in interaction were solved (3). To date, neither the spatial organization nor the stoichiometric composition of the entire complex in live cells was clarified. Using live cell FRET–FLIM and FCCS approaches with fluorescent protein-tagged subunits, we demonstrated a 1:1:1 stoichiometry of the three subunits, estimated their affinity, and analyzed their spatial organization. Finally, we used these findings to elaborate a new 3D *in silico* model of the entire cytosolic complex in the live cell situation. This model shows an elongated complex and a flexible hinge. It is fully compatible with the multiple steps of oxidase activation. In addition, it can guide the identification of potential sites for anti-inflammatory drug targets to regulate the NADPH oxidase activity.

Results

FP-tagged subunits are correctly expressed and are functional

The cytosolic subunits $p40^{phox}$, $p47^{phox}$, and $p67^{phox}$ were tagged with fluorescent proteins (FPs; Table S1), either cyan (CFP: mTurquoise or Aquamarine) (7), yellow (YFP: Citrine) (8), or red (RFP: mCherry) (9). The size of the fusion proteins expressed by COS7 cells was verified by Western blotting (Fig. S1*A*). To assess whether the FP-labeled subunits are able to reconstitute the active oxidase complex, we used $COS^{Nox2/p22}$ cells stably expressing the membranous subunits $Nox2/p22^{phox}$ and Rac, but no endogenous cytosolic subunits (10). $COS^{Nox2/p22}$ were transiently transfected with the three cytosolic subunits with or without a FP tag (Fig. 2*A*). The production of superoxide anions was monitored by a luminometry assay sensitive to extracellular ROS (Fig. 2*B*). The ROS production started upon activation with

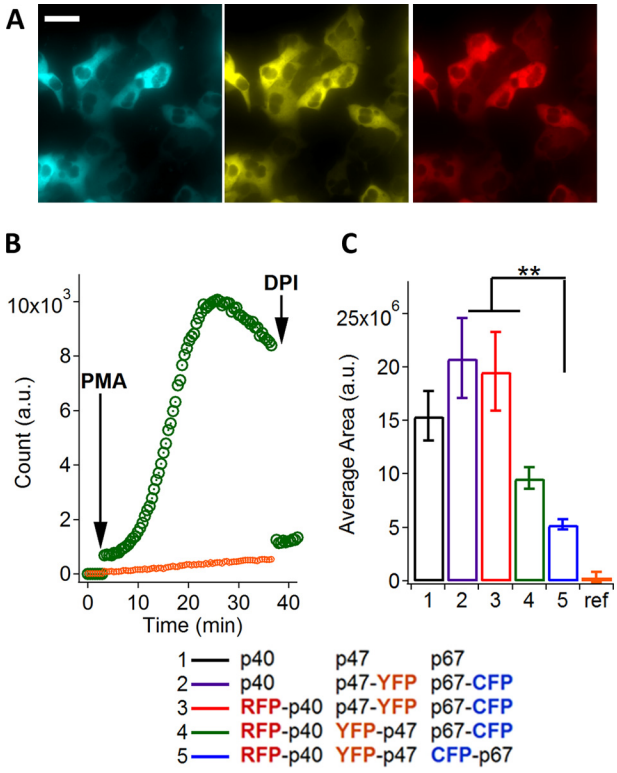

Figure 2. FP-tagged subunits form a functional oxidase. *A*, images of triple-transfected $COS^{Nox2/p22}$ cells expressing $p47^{phox}$-CFP, $p67^{phox}$-YFP, and RFP-$p40^{phox}$ subunits (*left* to *right*). *Scale bar*, 20 μm. Five conditions of $p40^{phox}$, $p47^{phox}$, and $p67^{phox}$ with no tag, two, or three tags on either N or C terminus were tested. *B*, time course of the luminescence signal (L-012 + horseradish peroxidase) from triple-transfected $COS^{Nox2/p22}$ cells stimulated by PMA and stopped by the oxidase inhibitor DPI at the indicated times (condition 4, *green*). In *orange*, the signal obtained with nontransfected cells as reference. *C*, integrated PMA-stimulated luminescence signal over 30 min ($n = 3$; means ± S.E.). **, $p < 0.01$, Tukey's multiple comparison test.

phorbol myristate acetate (PMA) and stopped immediately after addition of diphenyleneiodonium (DPI), a NADPH oxidase inhibitor. All constructs allowed a pronounced ROS production (Fig. 2*C*). The production with N-terminal tagged $p47^{phox}$ and $p67^{phox}$ was lower compared with the C-terminal tagged variants but still much higher than the nontransfected cells. The presence of the FP tags slowed down the ROS production and consequently delayed the time point at which the maximal signal was reached (Fig. S1, *B* and *C*). Taken together, these observations show that all our FP-tagged subunits are able to reconstitute an active NADPH oxidase complex and are fully suitable to explore their spatial organization and affinity.

FRET is observed between fluorescent proteins at both ends of individual subunits and is not strongly modified in presence of their partners. We then tagged each of the cytosolic subunits $p40^{phox}$, $p47^{phox}$ and $p67^{phox}$ simultaneously at both termini with a donor (D) and an acceptor (A) FP for FRET, resulting in so-called tandems (Fig. 3 and Table S1). We used as a positive control a simple D/A tandem in which the donor and acceptor FPs were linked by a flexible 27-amino acid-long peptide (11). Tandems were expressed in COS7 cells, and FRET was monitored by FLIM. The apparent FRET efficiencies, E_{app}, were derived from the average fluorescence lifetime of the donor FP measured in individual cells (Equations 1–4 under "Experimental procedures"). E_{app} values for the $p40^{phox}$, $p47^{phox}$, and

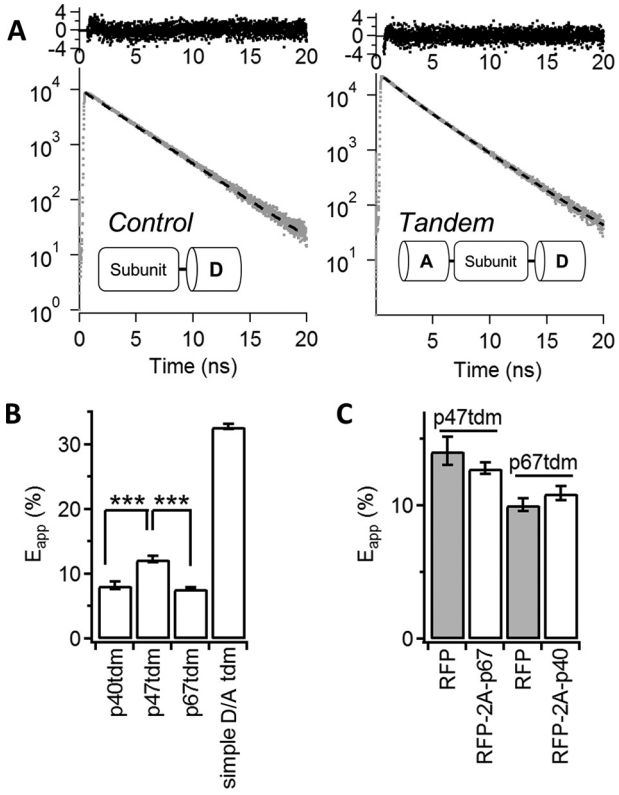

Figure 3. Efficient FRET between N- and C-terminal tags on all subunits (tandem). *A*, representative example of fluorescence decays of the tandems and their fits (*dashed line*). The *upper panels* show the residual difference plot. For p40^{phox}, a YFP/RFP FRET pair was used, whereas p47^{phox}, p67^{phox}, and the simple D/A tandem were labeled with a CFP/YFP FRET pair. The control shown on the *left* is p40^{phox}-YFP (τ_{donor} = 3.18 ns, χ^2 = 1.12), whereas the tandem shown on the *right* is RFP-p40^{phox}-YFP (τ_{long} = 3.17 ns, τ_{short} = 1.56 ns, accounting for 77 and 23% of the decay amplitude, respectively, χ^2 = 1.09). *B*, apparent FRET efficiencies for p40^{phox}, p47^{phox}, and p67^{phox} tandems and the positive control (simple D/A tandem). *C*, effect of p67^{phox} co-expression on the p47^{phox} tandem and of p40^{phox} on the p67^{phox} tandem. A co-transfection of the tandem with RFP alone was used as control (n = 10–30 cells; means ± S.E., raw data Fig. S2). ***, $p < 0.001$, Tukey's multiple comparison test.

p67^{phox} tandems were significant, although lower than in the simple D/A tandem (E_{app} = 8.2 ± 1.2%, 12.3 ± 1.2%, 7.7 ± 1.1%, and 32.7 ± 1.8%, respectively; Fig. 3*B*). The low E_{app} values for the subunit tandems are consistent with the much larger size of the central subunits as compared with a 27-amino acid peptide linker.

Next, we studied the influence of the p67^{phox} partner on the p47^{phox} tandem and of p40^{phox} on the p67^{phox} tandem. Either p47^{phox} or p67^{phox} tandems were co-expressed with a plasmid coding for the partner subunit connected to RFP via the viral P2A peptide (12, 13). The P2A sequence prevents the peptide bond formation and leads to the separate expression of the subunit and the RFP, the presence of the RFP proving the correct expression of the partner subunit. The co-expression of tandems with RFP alone was taken as reference (Fig. 3*C*). The co-expression of RFP-2A-p67^{phox} did not change the apparent FRET efficiency in the p47^{phox} tandem, and similarly, the presence of p40^{phox} did not modify the FRET level of the p67^{phox} tandem (Fig. 3*C* and Fig. S2), showing that in both cases, the overall geometry of the tandem is not significantly modified upon interaction with their partners.

FRET signals indicate specific interaction between p67^{phox} and p47^{phox} and provide information on their spatial organization

The bimolecular interaction between FP-tagged cytosolic subunits was then investigated using similar FLIM-FRET methodologies (Fig. 4). First, we studied the interaction of p67^{phox} and p47^{phox} (Fig. 4, *A–C* and *F*). Upon co-expression of p47^{phox}-CFP/p67^{phox}-YFP, the lifetimes of the CFP donor were on average significantly shorter than the reference value for p47^{phox}-CFP alone (Fig. 4, *A* and *B*). However, as usual in dual expression systems, FRET efficiencies E_{app} varied strongly from cell to cell, depending on the amount of expressed acceptor. We thus determined E_{app} as a function of the acceptor quantity, as estimated from its average fluorescence intensity (Fig. 4*C*), or as a function of the ratio [A]/[D] (Fig. 4*F*), using a custom calibration procedure (see supporting information), as shown by others (14, 15). In all cases, the FRET efficiency increases with the absolute or relative amount of acceptor.

For p47^{phox} and p67^{phox} subunits labeled at their C termini (CC labeling), E_{app} reaches a maximum value ~12% at high acceptor levels (Fig. 4, *C* and *F*). This is significantly higher than the negative control, consisting of the co-expression of p47^{phox}-CFP with YFP alone (Fig. 4*C* and Fig. S3*A*). As a second negative control, we used a truncated version of p47^{phox} missing the PRR domain (p47^{phox}ΔCter [1–342]) and leading *in vitro* to a complete abrogation of any interaction with p67^{phox} (16). The co-expression of p47^{phox}ΔCter-CFP with p67^{phox}-YFP gives clearly different FLIM images as compared with p47^{phox}-CFP, with well-separated average lifetime distributions (Fig. 4, *A* and *B*), and measured E_{app} values in the range of the first negative control (Fig. 4*C* and Fig. S3*A*). The observation of a plateau value for E_{app}, well above the values of the controls, provides strong evidence for a specific interaction (17). The absence of significant FRET in the case of p47^{phox}ΔCter shows in addition that the PRR domain of p47^{phox} is required for this interaction in live cells.

We then modified the labeling sites of our FP tags, either by switching them to the N termini or by exchanging FP colors between p47^{phox} and p67^{phox} (Fig. 4, *C* and *F*). For the CN tags, the maximum E_{app} of 8% was lower than for the CC labeling (Fig. 4*F*), yet significantly above the negative controls (Fig. S3*A*). For the NN tags, E_{app} values remained very low and close to the range of the negative controls (Fig. 4*C* and Fig. S3*A*).

To evaluate independently the occurrence of an interaction between p47^{phox} and p67^{phox} tagged at their N termini, we used FCCS. In this technique, the fluctuations of the fluorescence intensities of FP-tagged p47^{phox} and p67^{phox} diffusing in and out a confocal volume in the cytosol of COS7 cells are analyzed by auto- and cross-correlation functions (see "Experimental procedures"). A cross-correlation function with a non-null amplitude was observed for p47^{phox} and p67^{phox} tagged either at their CC and NN termini (Fig. 5*A*), showing in both cases a co-diffusion of the fluorophores indicative of complex formation.

We thus observe a specific interaction between p47^{phox} and p67^{phox} cytosolic subunits for all tested positions and types of FP tags, with in most cases E_{app} well above negative controls. Apparent FRET efficiencies measured in living cells are very

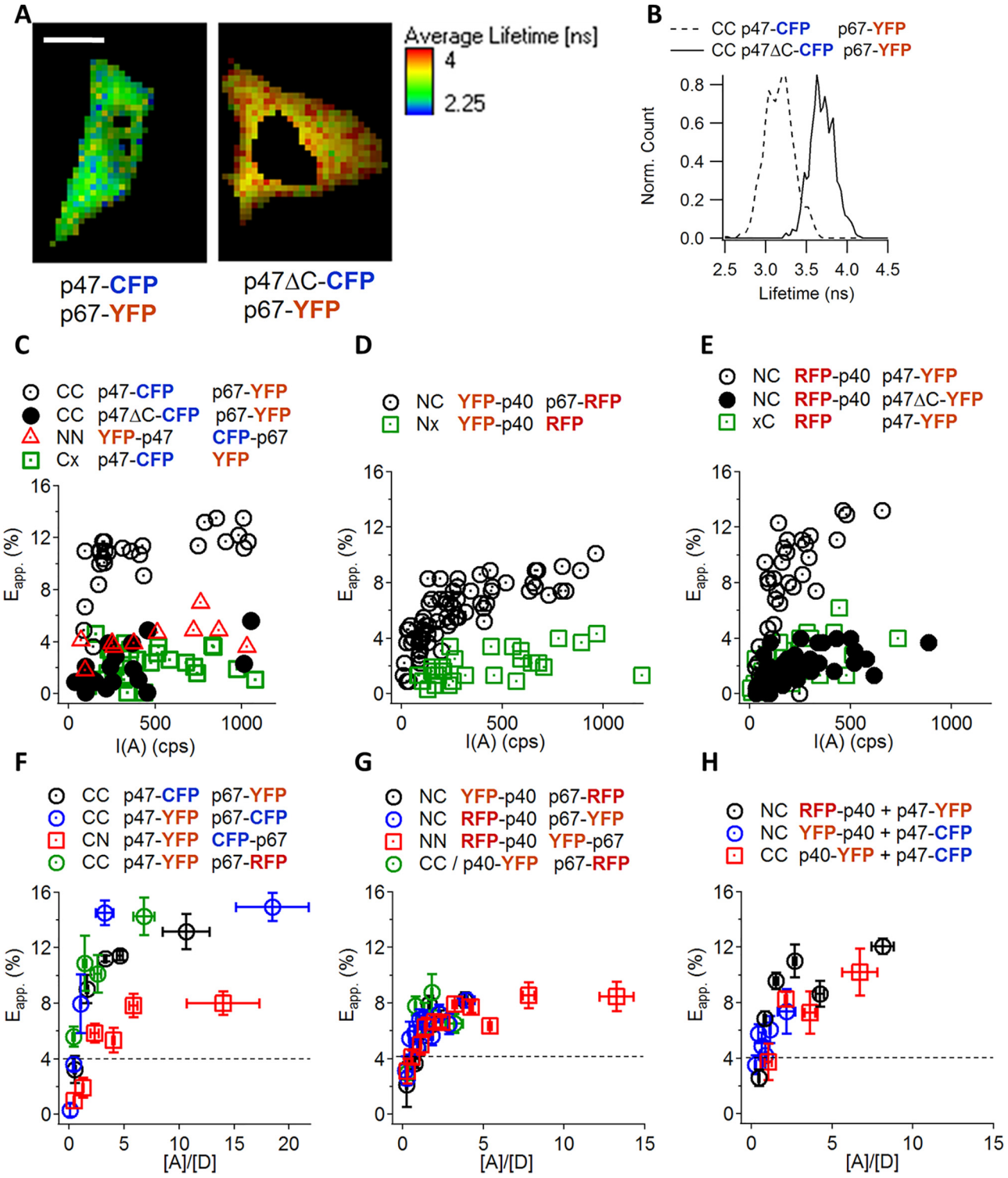

Figure 4. FRET reveals heterodimer formation between all subunits. *A*, representative fluorescence lifetime images of COS7 cells expressing p47-CFP (*left panel*) or p47ΔC-CFP with p67-YFP (*right panel*). *Scale bar*, 10 μm. *B*, corresponding histograms of fluorescence lifetimes over the image pixels. The lifetime of p47-CFP (donor alone) is 3.95 $\pm$ 0.05 ns. *C–E*, FRET efficiencies plotted against acceptor intensity. Each *symbol* represents the value for one cell. *F–H*, FRET efficiencies plotted against acceptor/donor ratio. Each *symbol* represents the mean $\pm$ S.E. of three to six cells. The *dashed lines* indicate the upper limit of the negative controls shown as *green squares* in *C–E*. *Left panels* of *C* and *F*, interaction of $p47^{phox}$ and $p67^{phox}$; *center panels* of *D* and *G*, interaction of $p40^{phox}$ and $p67^{phox}$; *right panels* of *E* and *H*, interaction of $p40^{phox}$ and $p47^{phox}$.

complex average quantities. In addition, the efficiency of energy transfer depends on both the distance and relative orientation between the donor and the acceptor, as predicted by Förster theory (see "Experimental procedures"). Because the fluorescent proteins are attached to the subunits through variable flexible linkers (Table S1), a large range of relative FP orientations are likely allowed, leading to some averaging of the orientation factor. In the frame of this paper, we will thus assume that major

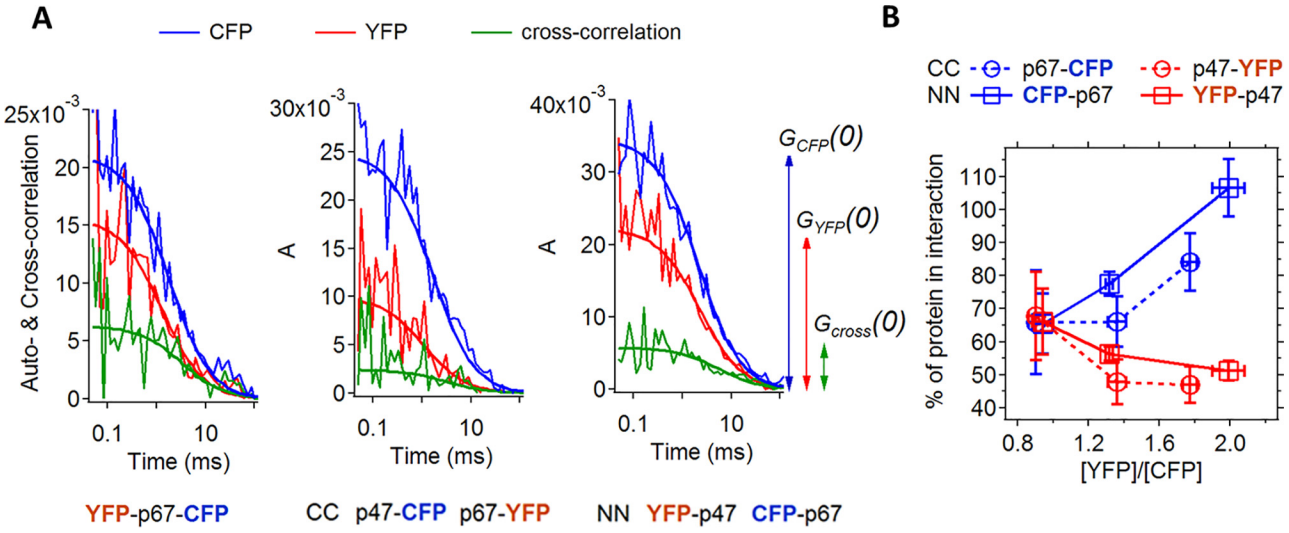

Figure 5. FCCS demonstrates that all p67^{phox} is in complex with p47^{phox}. *A*, example of auto-correlation and cross-correlation functions and their fits from individual cells. Shown are FCCS data from COS7 cells transfected with the p67^{phox} tandem (*left panel*) or p47^{phox} together with p67^{phox} (*middle* and *right panels*). We use the p67^{phox} tandem as a positive control for co-diffusion. *B*, fraction of protein in interaction, as a function of YFP:CFP ratio, as obtained from the correlation functions. At 2-fold excess of p47-YFP, all p67-CFP is in complex, and 50% of p47-YFP is in complex. Each *symbol* represents the means ± S.E. of five to ten cells from three independent experiments. We chose cells expressing YFP-tagged p47^{phox} in varying quantities while keeping the CFP-tagged p67^{phox} concentration at a nearly constant low level. This simulates the situation in neutrophils, where the expression of p47^{phox} is higher than p67^{phox} (32).

differences in FRET efficiencies are chiefly governed by distance. This is supported by the similar FRET efficiencies observed when different D/A pairs are used or when the anchoring sites of donor and acceptor are swapped (see for example Fig. 4, *C* and *F*). In this frame, the relative FRET efficiencies observed for donor and acceptor located at different termini provide interesting topological information. The maximum apparent FRET efficiency is higher for the CC labeling than for the CN labeling (Fig. 4*F*). Indeed, the two C termini are known to bind to each other and should be closer than the N terminus of p67^{phox} and the C terminus of p47^{phox}, which are separated by p67^{phox} itself (Fig. 1). For the NN labeling, the distance between FPs is most likely too large to observe FRET, because we have evidence for complex formation through FCCS. The upper distance limit for a FRET-positive situation is approximately twice the Förster radius of the FRET pair (see "Experimental procedures"), ~100 Å. To fulfill this distance condition, the N termini of both subunits should point to opposite directions in the complex.

FRET signals indicate specific interactions between p40^{phox} and p67^{phox} and between p40^{phox} and p47^{phox}

We studied similarly the interactions between FP-tagged p40^{phox} and p67^{phox} (Fig. 4, *D* and *G*, and Fig. S3*B*). For all tag positions (NC, NN, or CC), specific FRET was observed with the same maximum efficiency, ~8% at the plateau (Fig. 4, *D* and *G*). The similar maximum FRET efficiencies indicate comparable distances between the different termini of p40^{phox} and p67^{phox}.

The direct p40^{phox}–p47^{phox} interaction was questioned to be of physiological relevance or to be rather an artificial phenomenon resulting from test tube experiments in the absence of p67^{phox} (4). The possible interaction sites were identified *in vitro* to be the SH3 domain of p40^{phox} and the C-terminal PRR domain of p47^{phox}, which is also the binding site for p67^{phox} (Fig. 1). We co-expressed p40^{phox} and p47^{phox} or its truncated version p47^{phox}ΔCter with NC or CC labeling (Fig. 4, *E* and *H*). We found specific FRET in both cases with equivalent E_{app}, which indicates that the FP tags at both termini of p40^{phox} have a similar average geometry relative to the C terminus of p47^{phox}. When p47^{phox}ΔCter was used instead of full-length p47^{phox}, no significant FRET was observed (Fig. 4*E* and Fig. S3*C*). This confirms the requirement of the PRR domain of p47^{phox} for the interaction with p40^{phox} in live cells.

The cytosolic complex has a 1:1:1 composition with a high affinity between the subunits

FRET depends strongly on the number of acceptors in the direct vicinity of the donor and thus allows exploration of the stoichiometry of the interaction (18). An uneven stoichiometry of the subunits in the complex (X:Y) will result in different maximum E_{app} when the donor and acceptor are swapped between subunits (Fig. S4). In contrast, even subunit ratios (X:X) will give the same maximum E_{app}. On heterodimers formed by p47^{phox}/p67^{phox}, as well as by p40^{phox}/p67^{phox}, swapping donor and acceptor did not change the maximum apparent FRET efficiency (Fig. 4, *F* and *G*). We also investigated possible homodimerization of the cytosolic subunits by co-expressing each subunit tagged with donor and acceptor FPs in the same cell. In all cases, the E_{app} scatters in the range of the negative controls (Fig. S5), indicating that there are no detectable homodimers. Taken together, our findings support a 1:1:1 stoichiometry for the cytosolic complex in the living cell, in agreement with *in vitro* experiments (19, 20).

The amplitudes of the auto- and cross-correlation functions obtained by FCCS provide an estimate of the relative expression levels of the FP-tagged subunits and of their fraction in interaction ("Experimental procedures" and supporting information). The FCCS analysis gives qualitatively similar results with FRET-positive CC labeling or FRET-negative NN labeling (Fig.

5*B*). In both cases, the fraction of interacting protein is correlated to the relative expression level of the proteins. Although all p67^{phox} is bound in complex in the presence of a 2-fold excess of p47^{phox}, the fraction of p47^{phox} interacting with p67^{phox} decreases concomitantly. The apparent fraction of molecules in interaction is somewhat lower for the FRET-positive CC labeling than for the FRET-negative NN labeling, which may be ascribed to a FRET-induced decrease of the amplitude of the cross-correlation function (21).

The concentration of bound and free diffusing p47^{phox} and p67^{phox} obtained from the FCCS measurement can also be used to estimate their apparent dissociation constant, K_D^{app} (see supporting information). The median K_D^{app} value is in the range of a few hundred nanomolar, showing a high affinity between p47^{phox} and p67^{phox} in live cells. Such a high affinity, with a K_D well below 1 μM, is consistent with previous values obtained *in vitro* ranging from 4 to 32 nM (22).

In conclusion, FRET imaging and FCCS experiments in live cells clearly demonstrate specific interactions between the three cytosolic subunits of the NADPH oxidase and give new insights into their spatial organization in the complexes. In the next paragraphs, we will use this information, together with SAXS, NMR, and X-ray crystallography data, to build a 3D model of the heterotrimer. The crystallographic structure of p40^{phox} was solved (5), but p47^{phox} and p67^{phox} are highly flexible, and only some domains were crystallized. First, we will describe how several putative conformations of p67^{phox} and p47^{phox} were selected from SAXS experiments. Second, we will assemble the individual subunits and choose along this process the most appropriate conformation of p47^{phox} and p67^{phox}, with the help of the topological information obtained from FRET, to finally propose a 3D model of the heterotrimer compatible with our live cell experiments, as well as structural and biochemical results available in the literature.

Sets of models for p67^{phox} and p47^{phox} based on SAXS experiments

SAXS analysis consists in producing a set of atomic models compatible with the experimental SAXS curves using existing high-resolution structures of the crystallized domains, as explained under "Experimental procedures." For p67^{phox}, we re-examined previous experimental SAXS results (23), whereas new experiments were performed for the truncated p47^{phox}ΔCter [1–342] and for p47^{phox} to improve the model previously proposed by Durand *et al.* (24). For each of the three proteins, we retained a representative selection of possible models, which are discussed in the following steps.

The representative models of p47^{phox}ΔCter [1–342] were first examined to find a model adopting a relative orientation of its PX domain with the SH3 domains compatible with all other previous experimental observations (Fig. S6). First, in the resting state, p47^{phox} adopts an autoinhibited conformation in which the residues of the PX domain that interact with membrane phospholipids during the active phase are poorly accessible (25). Most of the models were rejected using this criterion (Fig. S6, *A* and *B*). Second, the PX domain interacts with the lateral surface of N-terminal SH3 domain including Arg-162 and Asp-166 (16, 25). Therefore, the latter two residues have to

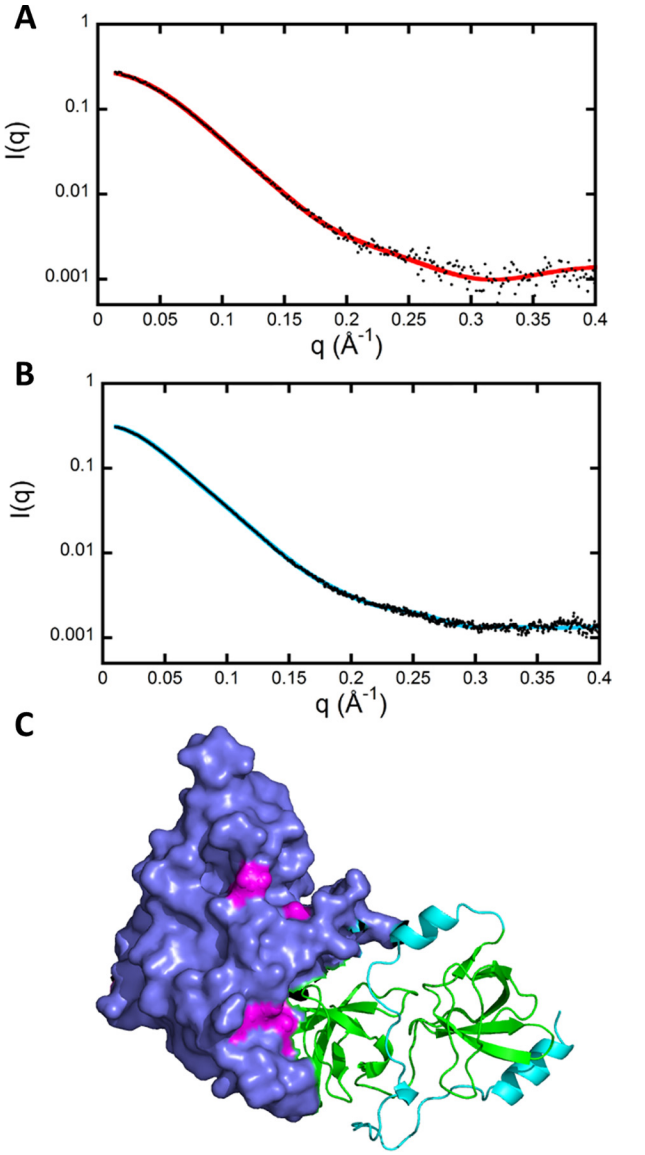

Figure 6. Modeling of p47^{phox}ΔCter from SAXS data. *A*, experimental SAXS curve measured on p47^{phox}ΔCter (*black dots*), compared with the calculated curve (*red line*) obtained from the selected model shown in *C* using the program CRYSOL (χ^2 = 0.97). *B*, experimental SAXS curve measured on full-length p47^{phox} (*black dots*) compared with the theoretical curve (*blue line*) calculated from the model of p47^{phox} shown in Fig. 7 (χ^2 = 1.25). *C*, selected SAXS model of p47^{phox}ΔCter that fulfills all the criteria discussed in the text and in Fig. S6. The PX domain is in *violet*, the SH3 domains are in *green*, and the AIR domain is in *cyan*. Residues of the PX domain responsible for interaction with the membrane in the activated form are shown in *pink*.

be located at the interaction surface between PX and SH3 domains (Fig. S6*C*). Third, previous kinetic analysis of hydrogen/deuterium exchange coupled to MS identified the residues involved in the intramolecular interaction in the resting state of p47^{phox}, which should also be masked (16).

We finally retained one model of p47^{phox} ΔCter that corresponds to all these criteria (Fig. 6*C*). The SAXS curve calculated on this model using the program CRYSOL is shown in Fig. 6*A* together with the experimental data (26). This model of truncated p47^{phox} was then used as starting point for the fit of the experimental SAXS pattern of the full-length p47^{phox} protein (Fig. 6*B* and Table S4), resulting in a set of

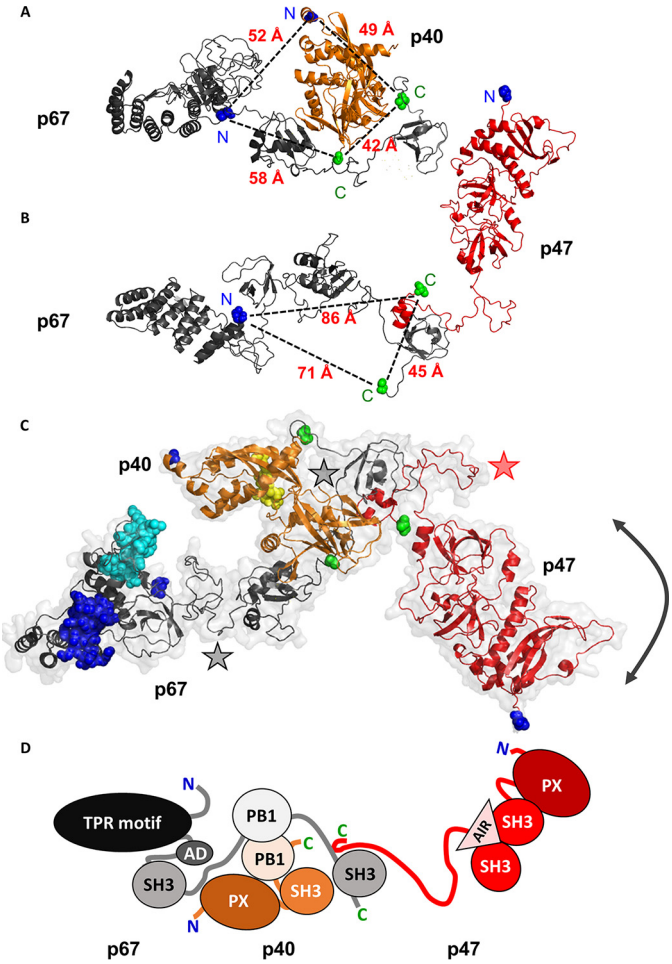

Figure 7. Proposed model of the complete cytosolic complex of phagocyte NADPH oxidase in the inactive state. *A–C*, ribbon representations of p40^{phox} (*orange*), p47^{phox} (*red*), and p67^{phox} (*gray*). The N termini are labeled in *blue*, and the C termini are labeled in *green*. Pairwise interactions are shown between p40^{phox} and p67^{phox} (*A*) and between p47^{phox} and p67^{phox} (*B*), whereas the whole 3D model of the heterotrimer is shown in *C*. Distances between termini, as predicted from the proposed model, are only given for model evaluation (see text). The *arrow* symbolizes the angular flexibility of the globular N-terminal domain of p47^{phox}. The *stars* indicate the flexible regions in p67^{phox} (*black stars*) and in p47^{phox} C terminus (*red star*). In p67^{phox}, *blue* and *cyan spheres* represent the Rac-binding β-hairpin insertion and the activation domains, respectively. The residues of the PX domains interacting with lipids in p40^{phox} are the *yellow spheres*. *D*, schematic representation of the complex showing the different functional domains.

full-length models carrying a mainly unstructured C-terminal part. Representative models of the full-length p47^{phox} protein were selected to build the whole 3D model of the heterotrimer in the next section.

Step-by-step assembly of a 3D model of the NADPH oxidase cytosolic complex

Assuming a 1:1:1 stoichiometry, the representative SAXS models of full-length p47^{phox} and p67^{phox} selected above and the crystal structure of p40^{phox} were then used to build a model of the heterotrimer, following a step-by-step workflow presented in Fig. S7. We know that p40^{phox} and p67^{phox} interact via their PB1 domains (Fig. 1), and the crystal structure of the p40^{phox}-PB1–p67^{phox}-PB1 interaction has been solved (27). This was used as a template to add first the whole crystal structure of p40^{phox} onto p67^{phox}-PB1 (5) (step I in Fig. S7). Then we added on the p67^{phox}-PB1 domain the full-length p67^{phox} structural models previously selected. We selected the most appropriate model based on the following criteria, illustrated in Fig. S8. First, we kept the models that had neither clashes nor sterical hindrance with p40^{phox}. Second, considering the maximum dimension of p67^{phox} determined by SAXS (D_{max} = ~160 Å; Table S4) (23, 28) and moreover the observation of significant FRET between the two termini of p67^{phox} in the p67^{phox} tandem, the N terminus of p67^{phox} has to be bent toward its C terminus. Third, for the p40^{phox}–p67^{phox} interaction, the significant and comparable FRET efficiencies for all tag positions (Fig. 4*G*) indicates that the termini of p40^{phox} and of p67^{phox} are at similar distances and significantly below the maximum FRET-compatible distance of 100 Å. The later condition is only fulfilled when p40^{phox} and p67^{phox} adopt a cross-like spatial arrangement (Fig. S8). A representative p67^{phox} SAXS model compatible with all three criteria was selected (step II in Fig. S7).

The resulting model of the p40^{phox}–p67^{phox} complex became the starting point to add p47^{phox}. The full-length p47^{phox} SAXS models were added with the help of the NMR structure of the interaction between the C termini of p47^{phox} and p67^{phox}, which are bound via their PRR (p47^{phox}) and SH3 (p67^{phox}) domains (29) (step III in Fig. S7). Most of our full-length p47^{phox} SAXS models lead to steric clashes with p40^{phox} and/or a distance between the N termini of p47^{phox} and p67^{phox} that is too short to account for the absence of clear FRET observed for NN labeling of these two subunits (Fig. S9). This leads to the selection of a p47^{phox} SAXS model where p47^{phox} points in the opposite direction of p67^{phox} in a tail-to-tail orientation. This last step results in the complete 3D model of the p40^{phox}–p47^{phox}–p67^{phox} heterotrimer (step IV in Fig. S7 and Fig. 7).

Evaluation of our proposed 3D model: significant features and consistency with experimental data

Our assembled model of the NADPH oxidase cytosolic complex reveals an elongated structure where functional domains are connected by flexible peptide linkers (Fig. 7). As already stated, the proposed cross-like arrangement of p40^{phox} and p67^{phox} leads to distances between their termini compatible with significant and equivalent FRET for all combinations (Fig. 7*A*). The interaction of p47^{phox} with p67^{phox} also brings their C termini in close vicinity, coherent with the high E_{app} measured for CC labeling, whereas the intermediate C–N distances are consistent with a lower E_{app} for the CN labeling (Fig. 7*B*). Interestingly, the FRET efficiency for the CN-tagged subunits is close to the one of the p67^{phox} tandem. Indeed, the C termini of p47^{phox} and p67^{phox} are very close and separated from the N terminus of p67^{phox} by a portion of p67^{phox} itself. On the other hand, p47^{phox} is expected to be elongated alone in solution (D_{max} by SAXS is in the order of 125 Å; Table S4), but the presence of intramolecular FRET in p47^{phox} tandems in live cells suggests that the subunit can adopt a more compact conformation. Indeed, the flexibility of its unstructured C terminus clearly allows movements of the N-terminal domain (featured by an *arrow* in Fig. 7*C*). The absence of FRET between NN-labeled p47^{phox} and p67^{phox} suggests that p47^{phox} cannot flip

completely toward p67^{phox} but might adopt either a more elongated or more condensed conformations, as well as different angles with respect to the long axis of p67^{phox}. Our model should thus be viewed as a relatively flexible structure with significant variability around its multiple hinges. The D_{max} values of p67^{phox} and the p67^{phox}–p40^{phox} complex are close (Table S2). The D_{max} values of p67^{phox}–p47^{phox} and p67^{phox}–p47^{phox}-p40^{phox} are similar as well (Table S2). This means that the presence of p40^{phox} does not change the overall dimensions of the complex. This is again consistent with the cross-like spatial arrangement of p40^{phox} with p67^{phox} and with the observation of the same E_{app} of the p67^{phox} tandem with or without p40^{phox}. Finally, we find that the calculated SAXS curves using the program CRYSOL on the p67^{phox}–p47^{phox}–p40^{phox} model is in reasonable agreement with the experimental curves published by Yuzawa *et al.* (Fig. S10) (28).

Discussion

Here we presented an integrated workflow to analyze the intermolecular interactions and the conformation of a complex of proteins formed by structured domains separated by unstructured segments in living cells. This analytical strategy may be adapted to any cytosolic protein complex composed of partially disordered subunits.

We first demonstrate the complementarity of FRET–FLIM and FCCS to characterize live cell interactions, estimate binding affinity, and obtain topological information using the same FP labeling for both techniques. This was made possible because of the new cyan variants mTurquoise and Aquamarine in the classical CFP/YFP FRET pair (7). Their increased brightness and photostability allowed both improved performances as donors for FLIM and full suitability for two-color FCCS experiments.

The dynamic NADPH oxidase complex depends on protein assembly for activation, and thus the development of inhibitors of this assembly is an attractive concept to regulate its activity (30, 31). For the p40^{phox}–p47^{phox}–p67^{phox} complex, there is a discrepancy between the 1:1:1 stoichiometry found in *in vitro* experiments (19, 20) and the 2–3 times higher expression level of p47^{phox} compared with p67^{phox} in neutrophils (32). In addition, this higher amount of p47^{phox} compared with p67^{phox} implies that p47^{phox} is present as both as free and a complex-bound subunit (32). However, it is not known whether free p67^{phox} exists. Our results revealed two pairwise interactions with a one to one stoichiometry, p47^{phox}–p67^{phox} and p40^{phox}–p67^{phox}, that strongly suggest that the ternary complex is assembled in a 1:1:1 stoichiometry inside a live cell. Furthermore, in the presence of an excess of p47^{phox}, all p67^{phox} were bound in complex. In solution, ~10–20% of recombinant p47^{phox} and p67^{phox} proteins have been detected as dimers (22). We did not observe any dimers by FRET–FLIM. Indeed, in live cells, the unbound cytosolic subunits may encounter a large diversity of potential partners that likely limits dimer formation.

Our live cell FRET results also provide topological information that nicely complements structural data from X-ray crystallography, NMR, and SAXS experiments obtained on purified recombinant proteins. The combination of SAXS data and single-molecule FRET *in vitro* is very useful to investigate protein folding by integrating complementary information (33–35). The combination of SAXS with FRET measurements of FP-labeled proteins *in cellulo* provides lower spatial and temporal resolution; however, it affords access to the conditions in living cells. To our knowledge, such an approach has not been described before. These pieces of information were integrated to build a new model of the cytosolic NADPH oxidase complex with several noticeable features: (i) p47^{phox} and p67^{phox} interact via their C termini in a tail-to-tail configuration, and their N termini are over 100 Å apart; (ii) p67^{phox} and p47^{phox} are not fully elongated; and (iii) p40^{phox} and p67^{phox} adopt a cross-like conformation (Fig. 7). The model is consistent with the idea that p47^{phox} is required for the initial assembly of the functional oxidase. Indeed, the PX domain and the SH3 domains of p47^{phox} are located on one end of the complex, ideally positioned to interact with phospholipids (PX domain) and with p22^{phox} (SH3 domains) to initiate oxidase assembly. This may then bring p40^{phox} and p67^{phox} closer to the membrane. Indeed, the PX domain of p40^{phox} also interacts with membrane lipids, and the N terminus of p67^{phox} requires several activation steps mandatory for superoxide production. The flexible hinge between the N-terminal half of p47^{phox} and the rest of the trimeric complex may be required to establish the initial contact with phospholipids and p22^{phox} and then bend the complex to bring p67^{phox} closer to Nox2. In addition, the proximity of the C terminus of p47^{phox} with the SH3 domain of p40^{phox} in the model raises the question of whether p40^{phox} contributes to stabilize the C terminus of p47^{phox} at the SH3 domain of p67^{phox}. The position of the p40^{phox} PX domain in the middle of the elongated complex is unfavorable for a role of this domain in the initiation of oxidase assembly because it would require a lateral attachment of the complex on the membrane. However, if p47^{phox} leaves the active complex as recently suggested (36), the p40^{phox} PX domain would be in a favorable position to bind to phosphoinositides in the membrane after its dissociation from PB1 (5), and this would help keeping p67^{phox} in place (37).

In p67^{phox}, the TPR and the activation domain are essential for the assembly with Rac and Nox2 and, ultimately, for activation of the oxidase. In the proposed model of the heterotrimer, presented here in the resting state (Fig. 7), the N-terminal region of p67^{phox} is well-exposed and accessible. We assume that the global orientation and the internal flexibility between its domains is fully compatible with the binding to Rac or to Nox2 through the activation domain (38). At this stage of characterization of the ternary cytosolic complex, it seems that the main limiting step toward activation is p47^{phox} that needs to be activated to promote assembly of the whole cytosolic complex at the membrane. Preventing the conformational changes of the N terminus of p47^{phox} would probably block the subsequent interactions with the membrane and p22^{phox} and prevent oxidase activation. Therefore, our approach provides critical information for the design of inhibitors that would interfere with key steps in the activation process. Furthermore, the data we obtained and the model are a starting point to investigate the changes that may occur during activation of the oxidase. They may also serve to compare WT subunits with mutations found

in patients with chronic granulomatous disease to understand the phenotype of this oxidase deficiency.

Experimental procedures

Plasmid library and transfection

Plasmids encoding full-length human p47^{phox} (NCF1) and p67^{phox} (NCF2) both embedded in a pEGFP-N1 vector (Clontech) (36) and p40^{phox} (NCF4) embedded in a CMD8 vector (gift from Marie Claire Dagher) were used as a starting point to build a full library of N- and C-terminal tagged fusion proteins. The cDNA of the subunits were cut out with restriction enzymes or amplified by PCR and inserted in either cyan mTurquoise or Aquamarine-N1 or -C1 vectors (variants of the pECFP vectors: mTurquoise: T65S/S72A/H148D/S175G/A206K (39), Aquamarine: T65S, H148G (40)), yellow Citrine-N1 or -C1 vectors (the mutation Q69M was introduced into EYFP) (8), or the red mCherry-C1 vector (Clontech, Takara Biotechnology, Co., Ltd.). The internal start codon (ATG) was removed by PCR from the FP-N1 vectors or from the subunits embedded in FP-C1 vectors. Table S1 displays an overview of the constructs. To build the plasmids coding for RFP-2A-p67^{phox} or p40 ^{phox}, we ordered a synthetic gene coding for mCherry-P2A (P2A = ATNFSLLKQAGDVEENPGP) (12) framed by AgeI and HindIII restriction sites (Eurofins). The two enzymes were used to cut out the FP and insert mCherry-2A in pECitrine-p67-C1 or pEmCherry-p40-C1. Primers were purchased from Eurogentec (Kaneka Corp., Tokyo, Japan). Plasmids were amplified in DH5α *Escherichia coli*, DNA was purified with E.N.Z.A.® mini kit 2 (Omega Bio.Tek). For transfection, cells (COS7 or COS$^{Nox2/p22}$) were seeded either on glass coverslips (Ø 25 mm, thickness of 0.13–0.16 mm) in 6-well plates for microscopy or in 24-well plates for luminometry 1 day before the experiment. The cells were transiently transfected with XtremeGene HP (Roche Diagnostics) following the supplier's instructions and used 24–48 h after transfection. Transfection efficiency, monitored by flow cytometry, was constantly between 20 and 30% for triple transfection. Based on the high reproducibility of transfection efficiencies, we assumed that the subunits without FP tag were present in the cells at the same average level as the FP-tagged ones.

Cell culture

COS7 cells were purchased from ATCC and cultured following the supplier's instructions. COS7 cells stably expressing Nox2 and p22^{phox} (COS$^{Nox2/p22}$) were kindly provided by M. Dinauer (Washington University School of Medicine, St. Louis, MO) and cultured in medium containing selecting antibiotics (10).

$O_2^{\cdot-}$ detection by L-012 chemiluminescence

L-012 (100 μM, Wako Chemicals) and horseradish peroxidase (20 units/ml) were mixed and added to the well containing transfected COS$^{Nox2/p22}$ cells a few minutes before the addition of 500 nM of PMA to stimulate the assembly of the NADPH oxidase. 20 μM of DPI was added to stop the $O_2^{\cdot-}$ production. The production was quantified as the relative light units area under the curve recorded during 30 min with a SynergyH1 plate reader (Biotek).

Fluorescence lifetime imaging microscopy

Time-resolved laser scanning TCSPC microscopy was performed on a custom made microscope as described previously (40). Briefly, the setup is based on a TE2000 microscope with a 60×, 1.2NA water immersion objective (Nikon). The epifluorescence pathway is equipped with an mercury lamp, a set of filter cubes for the different FPs, and a CCD camera (ORCA-AG, Hamamastu Photonics; Table S3). The TCSPC path is equipped with pulsed laser diodes (440 nm for CFPs; 466 nm for YFPs, PicoQuant) driven by a PDL800 driver (20 MHz, PicoQuant). The C1 scanning head (Nikon) probes a 100 × 100-μm maximum field of view. To select the FP fluorescence, dichroic mirrors and filter sets were used before the detection by a MCP-PMT detector (Hamamatsu Photonics). The signals were amplified by a fast pulse preamplifier (Phillips Scientific) before reaching the PicoHarp300 TCSPC module (PicoQuant). Counting rates were routinely between 50,000 and 100,000 counts/s. Transfected cells were kept in PBS at 20 °C and studied for 2 h maximum in an Attofluor cell chamber (Thermo Fisher Scientific).

The lifetime of a fluorophore is an intensive property, independent of its concentration, which can be precisely monitored even in live cells. A precision of a few percentages on lifetime is common (17, 41–44). The TCSPC fluorescence decay of all the pixels of the cytosol was computed by the SymPhoTime software (Fig. 3*A*). The decays were fitted with a monoexponential fit function (Equation 1) for the control cells expressing a donor fusion protein (without acceptor), the donor being Aquamarine, mTurquoise, and Citrine (Fig. 3*A*, *left panel*),

$$I(t) = I_0 e^{-\frac{t}{\tau_{donor}}} + C \quad \text{(Eq. 1)}$$

where C is the constant background. Because the donor has a monoexponential lifetime, its fluorescence decay in the presence of FRET to an acceptor can be fitted with a biexponential function (Equation 2, and Fig. 3*A*, *right panel*),

$$I(t) = \alpha_{long} I_0 e^{-\frac{t}{\tau_{long}}} + \alpha_{short} I_0 e^{-\frac{t}{\tau_{short}}} + C \quad \text{(Eq. 2)}$$

where C is the constant background. α_{long} and α_{short} are the proportions of a long (τ_{long}) and a short (τ_{short}) lifetime component, respectively. For fitting, we used a custom-made procedure in IGOR Pro (WaveMetrics). The quality of the fits is evaluated by the weighted residual distribution and Pearson's χ^2 test (Fig. 3*A*).

$<\tau_{DA}>$ is the average lifetime of the donor-fusion protein, D, in presence of an acceptor fusion protein, A (Equation 3).

$$<\tau_{DA}> = \alpha_{long}\tau_{long} + \alpha_{short}\tau_{short} \quad \text{(Eq. 3)}$$

The apparent FRET efficiency E_{app} is calculated using $<\tau_{DA}>$ and τ_{donor} (Equation 4).

$$E_{app} = 1 - \frac{<\tau_{DA}>}{\tau_{Donor} \times 100} \quad \text{(Eq. 4)}$$

It was calculated on a cell by cell basis from the fluorescence decays obtained for each cell using for τ_{donor} the lifetime of the same donor/subunit fusion protein alone.

The apparent FRET efficiencies measured in each cell are complex averages over highly heterogeneous populations of donor molecules engaged in different FRET interactions. Fundamentally, these FRET efficiencies depend on both the distance and relative orientation between donor and acceptor. The determination of distances between FRET partners thus requires some assumption on the orientation factor κ^2 (45). Unfortunately, the *dynamic* isotropic regime leading to the popular value $\kappa^2 = 2/3$ cannot be applied to fluorescent proteins, because their rotational correlation time in water is ~14 ns *i.e.* three to four times longer than the lifetime of the donor excited state (46, 47). In the viscous environment of living cells, FPs must be considered as *static* on the time scale of the FRET interaction. On the other hand, because FPs are fused to the subunits through flexible linkers, they are expected to adopt a whole set of conformations, leading to broadly distributed, but probably nonisotropic and nonhomogeneous relative orientations and distances. Therefore, the precise calculation of distances from our FRET data, as proposed for example by Vogel *et al.* (48), is mostly out of reach. Instead, we used the apparent FRET efficiencies to establish distance limits, to guide topological reasoning, or to provide comparative information. Indeed, whatever the effective value of κ^2, the observation of a significant FRET indicates some proximity within the range of the critical Förster distance $R°$. Typical Förster distances of most fluorescent protein FRET pairs, calculated using $\kappa^2 = 2/3$, lie in the range of 50–60 Å (48). $R°$ evolves as $(\kappa^2)^{1/6}$ and thus varies only slowly with the orientation factor. Using $\kappa^2 = 0.476$, a value applicable to fully isotropic and homogeneous static averaging (17, 45, 49), we obtain quite similar values of $R° = 57$ Å for Aquamarine/Citrine and 55 Å for Citrine/mCherry. For the maximum but highly unlikely value $\kappa^2 = 4$, these distances would at most extend to 81 and 78 Å, respectively. In cases of unfavorable relative orientations, $R°$ could on the contrary decrease significantly below 50 Å. Conversely, as the D/A distance approaches twice $R°$, the FRET efficiency will tend virtually to 0. As a rule of thumb, assuming some degree of orientational and conformational averaging, and considering our practical detection limits, we took 100 Å as the upper distance limit to observe FRET in this study.

The FP-tagged subunits are transiently expressed, and the level of expression may strongly vary between cells. We recorded intensity images before any FLIM experiments on the same field of view. The intracellular concentrations are proportional to the average fluorescence intensities. E_{app} was commonly plotted as a function of the fluorescence intensity of the acceptor in the cell, and $I(A)$ was plotted to observe a FRET-positive situation (17, 50–53). As a negative control, the donor/subunit fusion protein was co-expressed with the free acceptor. This control is useful to (i) determine whether E_{app} is significant and (ii) to set the threshold for the maximum value of $I(A)$ beyond which unspecific FRET caused by molecular crowding starts to contribute to the signals. Indeed, when the cells are crowded with the acceptors, $I(A)$ becomes very high, and the donors show unspecific FRET with the acceptors nearby just because of the spatial proximity (17). We discarded such cells.

The plotting of E_{app} against $[A]/[D]$ required the calibration of fluorescence intensities measured in both donor and acceptor channel. The ratio of fluorescence intensities, $I(A)/A(D)$, was transformed in the concentration ratio of fluorescent proteins, $[A]/[D]$, using a custom calibration procedure of the microscopy setup (see supporting information and Figs. S11 and S12).

Fluorescence cross-correlation spectroscopy

A confocal microscope Leica TCS SP8 SMD (Leica Microsystems) was used. It is equipped with a DMI 6000 CS stand and a 63×/1.2 HC PL APO water immersion objective, a continuous argon laser (514 nm from Leica TCS SP8), and a diode pulsed laser (440 nm, PicoQuant). The signal was selected by 505-nm dichroic mirror and two bandpass filters (BP 478/22, BP 540/30) and detected by two APD detectors (PicoQuant). For the detection, the SMD module is constituted of a PicoHarp3000 system for TTTR mode of single photon counting (PicoQuant). The cells were kept in an air-conditioned chamber at 30 °C. To correct for the cross-talk between the CFP and YFP detection channels on the amplitudes of the correlation functions, we used a variant of fluorescence correlation spectroscopy called fluorescence lifetime correlation spectroscopy (54). The fluorescence signal of each channel was corrected from spectral bleed-through using fluorescence lifetime correlation spectroscopy filters as described elsewhere (55, 56). In this method combining TCSPC and FCS, the different FCS contributions are separated by using the different fluorescence decay pattern of both fluorophores. The fluctuations of fluorescence intensity were auto- and cross-correlated, and the resulting curves were analyzed using a standard pure diffusion model with SymphoTime (PicoQuant).

The auto-correlation function of fluorescence fluctuations returns the time needed for the fluorophore to cross-the confocal observation volume, V_{FP}, and the number of molecules, N_{FP}, present in V_{FP}. N_{FP} is the inverse of the amplitude to the auto-correlation function, $G_{FP}(0)$ (21). The concentrations of FPs in the observation volume are calculated as following where N_A is the Avogadro number (Equation 5).

$$[YFP] = \frac{1}{G_{YFP}(0)}\frac{1}{N_A}\frac{1}{V_{YFP}}, [CFP] = \frac{1}{G_{CFP}(0)}\frac{1}{N_A}\frac{1}{V_{CFP}} \quad \text{(Eq. 5)}$$

The amplitude of the cross-correlation function, $G_{cross}(0)$, allows the estimation of the concentration of the stoichiometric $p47^{phox}$–$p67^{phox}$ complex. $p47^{phox}$ and $p67^{phox}$ are respectively labeled with YFP and CFP (Equation 6).

$$[Complex] = \frac{G_{cross}(0)}{G_{YFP}(0)\cdot G_{CFP}(0)}\frac{1}{N_A}\frac{1}{V_{cross}} \quad \text{(Eq. 6)}$$

In practice, the observation volumes in the two channels, V_{YFP} and V_{CFP}, and V_{cross} have always different sizes and are not perfectly coincident. In addition, a fraction of FPs might be nonfluorescent because of nonmatured protein, dark state, or photobleaching (21). The later was kept here below 10%. To minimize the impact of these limits on the detection of inter-

actions, the fractions, X, of co-diffusing fluorophores that are also the fractions of protein in interaction, were normalized to the average fractions obtained for the p67^{phox} tandem, whose two tags diffuse together (Equations 7 and 8).

$$X_{YFP}^{cplx} = \frac{G_{cross}(0)}{G_{CFP}(0)} \left\langle \frac{G_{CFP}^{tandem}(0)}{G_{cross}^{tandem}(0)} \right\rangle \times 100 \quad \text{(Eq. 7)}$$

$$X_{CFP}^{cplx} = \frac{G_{cross}(0)}{G_{YFP}(0)} \left\langle \frac{G_{YFP}^{tandem}(0)}{G_{cross}^{tandem}(0)} \right\rangle \times 100 \quad \text{(Eq. 8)}$$

In addition, the relative amount of both partners was estimated as follows (Equation 9).

$$\frac{[YFP]^{cplx}}{[CFP]^{cplx}} = \frac{G_{CFP}(0)}{G_{YFP}(0)} \times \left\langle \frac{G_{YFP}^{tandem}(0)}{G_{CFP}^{tandem}(0)} \right\rangle \quad \text{(Eq. 9)}$$

The details for the computation of K_D^{app} can be found in the supporting information.

Protein preparation, SAXS data acquisition, and processing

p47^{phox} constructs were expressed as a GST fusion protein using a pGex-6P-1–derived vector containing the cDNA corresponding to the full amino acids sequence (from 1 to 397) for the full-length p47^{phox} or to a sequence coding for amino acids 1–342 for the p47^{phox}ΔCter construct lacking the C-terminal end of the protein after the AIR motif. For both constructs, the production protocol was the same. The proteins were expressed in *E. coli*, strain BL21(DE3). Expression was induced with 0.5 mM isopropyl β-D-thiogalactopyranoside, when the cell culture reached an OD of 0.6 at 600 nm. Temperature was then shifted to 20 °C for an overnight induction. The cells were harvested and resuspended in chilled lysis buffer (50 mM Tris, pH 7.5, 0.3 M NaCl, 1 mM EDTA, 2 mM DTT, and Complete EDTA-free protease inhibitor (Roche Diagnostics)). All following operations were carried out at 4 °C. The cells were disrupted by sonication and then centrifuged at 40 000 rpm for 40 min in a Beckman 45 Ti rotor. The supernatant was loaded onto a 4-ml gluthathione–Sepharose 4B column (GE Healthcare) equilibrated in the lysis buffer. Proteins were eluted at 1 ml/min with 50 ml of elution buffer (50 mM Tris, pH 7.5, 50 mM NaCl, and 10 mM glutathione). Fractions containing GST fusion of the corresponding p47^{phox} construct were pooled and digested overnight at 4 °C with PreScission protease (70 enzyme units per 40 mg of protein). Because of the genetic construction, digested p47^{phox} possesses 10 and 7 additional residues at its N and C terminus, respectively, and p47^{phox}ΔCter possesses only 10 additional residues at its N terminus. Digestion products were loaded at a flow rate of 1 ml/min onto a MonoS column (GE Healthcare) equilibrated in 50 mM Hepes, pH 7.5, 50 mM NaCl, 1 mM EDTA, and 2 mM DTT. The proteins were eluted with a 40-ml linear gradient of NaCl (50–500 mM). The resulting protein fractions containing the corresponding p47^{phox} construct were concentrated on a centrifugal concentration device with a 10-kDa cutoff. The protein was then diluted 20 times in 50 mM Hepes, pH 7.5, 100 mM NaCl, 1 mM EDTA, 2 mM DTT, and 5% glycerol and finally reconcentrated at different concentrations at which aliquots of p47^{phox}, or p47^{phox}ΔCter, were taken and stored for SAXS measurements. For p67^{phox}, p47^{phox}, and its truncated version, SAXS data processing led to a molecular mass close to that derived from the sequence showing that the protein solutions were devoid of oligomers (Table S4).

SAXS measurements on p47^{phox}ΔCter were performed on a laboratory instrument Nanostar (Bruker Nanostar, λ = 1.54 Å). SAXS data on full-length p47^{phox} were collected on the SWING beamline (SOLEIL synchrotron, St. Aubin, λ = 1.0Å). Both proteins were studied at different concentrations (Table S4). SAXS data were normalized to the intensity of the incident beam, averaged, and background-subtracted using the program package PRIMUS (57); intensities were put on an absolute scale using water scattering. The final pattern used for fitting was obtained by extrapolating to infinite dilution of the set of curves recorded at the different concentrations.

p47^{phox}ΔCter was modeled using the program BUNCH (58), which combines rigid-body and *ab initio* modeling approaches. The program starts from known structures of the two domains PX and SH3 tandem (Protein Data Bank code 1KQ6 and 1NG2, respectively) and finds the optimal positions and orientations of domains and probable conformations of the linkers by fitting the SAXS curve calculated on the model to the experimental curve. In a final step, we substituted the dummy residues of the linkers with all atom descriptions using the programs PD2 (59) and SCWRL4 (60). An ultimate adjustment was performed using the program CRYSOL. The modeling was repeated 100 times. Finally, models giving the best agreement with the experimental curve (lowest χ^2 values) were selected. The same approach was used for full-length p47^{phox} using the most probable model describing p47^{phox}ΔCter and the PRR domain (extracted from the Protein Data Bank code 1K4U) as a starting point. Models of p67^{phox} were built in the same way starting from the known structures (23). This modeling has shown that p67^{phox} is able to adopt a great variety of very different conformations. Not surprisingly the SAXS data can be fitted using an ensemble of models (EOM approach) (61). All SAXS data are shown in SASBDB (https://www.sasbdb.org)[6] under the SAS codes SASDEJ3, SASDEK3, and SASDEL3 (62).

Molecular structure alignment

Protein Data Bank structures and SAXS-based models were imported into the PyMOL Molecular Graphics System, version 1.8 Schrödinger, LLC.

Statistical analysis

The data are represented as means of at least three independent experiments ± S.E. Significance was tested with one-way ANOVA followed by a Tukey's multiple comparison test using GraphPad Prism version 5.

Author contributions—C. S. Z., L. B., M. T., and D. D. data curation; C. S. Z. formal analysis; C. S. Z., M. T., D. D., F. F., S. D.-C., and F. M. methodology; L. B., M. T., and D. D. investigation; F. M., O. N., and M. E. writing-review and editing; O. N. and M. E. conceptualization; O. N. and M. E. supervision; O. N. and M. E. funding acquisition; O. N. and M. E. project administration.

[6] Please note that the JBC is not responsible for the long-term archiving and maintenance of this site or any other third party hosted site.

Acknowledgments—COS$^{Nox2/p22phox}$ cells were a kind gift from Mary Dinauer. This work has benefited from the flow cytometry facility SpICy and the Microscopy Rennes Imaging Centre (MRic) for FCS measurements. We thank Julien Marcoux for the preparation of proteins for the SAXS experiments and Sophie Sacquin-Mora and Antoine Taly for fruitful discussion. We thank the staff of the SWING beamline for help during the SAXS measurements.

References

1. Uversky, V. N. (2016) Dancing protein clouds: the strange biology and chaotic physics of intrinsically disordered proteins. *J. Biol. Chem.* **291,** 6681–6688 CrossRef Medline
2. Pauwels, K., Lebrun, P., and Tompa, P. (2017) To be disordered or not to be disordered: is that still a question for proteins in the cell? *Cell. Mol. Life. Sci.* **74,** 3185–3204 CrossRef Medline
3. Sumimoto, H. (2008) Structure, regulation and evolution of Nox-family NADPH oxidases that produce reactive oxygen species. *FEBS J.* **275,** 3249–3277 CrossRef Medline
4. Massenet, C., Chenavas, S., Cohen-Addad, C., Dagher, M.-C., Brandolin, G., Pebay-Peyroula, E., and Fieschi, F. (2005) Effects of p47^{phox} C terminus phosphorylations on binding interactions with p40^{phox} and p67^{phox}: structural and functional comparison of p40^{phox} and p67^{phox} SH3 domains. *J. Biol. Chem.* **280,** 13752–13761 CrossRef Medline
5. Honbou, K., Minakami, R., Yuzawa, S., Takeya, R., Suzuki, N. N., Kamakura, S., Sumimoto, H., and Inagaki, F. (2007) Full-length p40^{phox} structure suggests a basis for regulation mechanism of its membrane binding. *EMBO J.* **26,** 1176–1186 CrossRef Medline
6. Piovesan, D., Tabaro, F., Paladin, L., Necci, M., Micetic, I., Camilloni, C., Davey, N., Dosztányi, Z., Mészáros, B., Monzon, A. M., Parisi, G., Schad, E., Sormanni, P., Tompa, P., Vendruscolo, M., *et al.* (2018) MobiDB 3.0: more annotations for intrinsic disorder, conformational diversity and interactions in proteins. *Nucleic Acids Res.* **46,** D471–D476 CrossRef Medline
7. Merola, F., Erard, M., Fredj, A., and Pasquier, H. (2016) Engineering fluorescent proteins towards ultimate performances: lessons from the newly developed cyan variants. *Methods Appl. Fluoresc.* **4,** 012001 CrossRef
8. Griesbeck, O., Baird, G. S., Campbell, R. E., Zacharias, D. A., and Tsien, R. Y. (2001) Reducing the environmental sensitivity of yellow fluorescent protein: mechanism and applications. *J. Biol. Chem.* **276,** 29188–29194 CrossRef Medline
9. Shaner, N. C., Campbell, R. E., Steinbach, P. A., Giepmans, B. N., Palmer, A. E., and Tsien, R. Y. (2004) Improved monomeric red, orange and yellow fluorescent proteins derived from *Discosoma* sp. red fluorescent protein. *Nat. Biotechnol.* **22,** 1567–1572 CrossRef Medline
10. Yu, L., Zhen, L., and Dinauer, M. C. (1997) Biosynthesis of the phagocyte NADPH oxidase cytochrome b_{558}: role of heme incorporation and heterodimer formation in maturation and stability of gp91^{phox} and p22^{phox} subunits. *J. Biol. Chem.* **272,** 27288–27294 CrossRef Medline
11. Betolngar, D.-B., Erard, M., Pasquier, H., Bousmah, Y., Diop-Sy, A., Guiot, E., Vincent, P., and Mérola, F. (2015) pH sensitivity of FRET reporters based on cyan and yellow fluorescent proteins. *Anal. Bioanal. Chem.* **407,** 4183–4193 CrossRef Medline
12. Kim, J. H., Lee, S.-R., Li, L.-H., Park, H.-J., Park, J.-H., Lee, K. Y., Kim, M.-K., Shin, B. A., and Choi, S.-Y. (2011) High cleavage efficiency of a 2A peptide derived from porcine teschovirus-1 in human cell lines, zebrafish and mice. *PLoS One* **6,** e18556 CrossRef Medline
13. Goedhart, J., van Weeren, L., Adjobo-Hermans, M. J., Elzenaar, I., Hink, M. A., and Gadella, T. W., Jr. (2011) Quantitative co-expression of proteins at the single cell level: application to a multimeric FRET sensor. *PLoS One* **6,** e27321 CrossRef Medline
14. Cardarelli, F., Bizzarri, R., Serresi, M., Albertazzi, L., and Beltram, F. (2009) Probing nuclear localization signal–importin α binding equilibria in living cells. *J. Biol. Chem.* **284,** 36638–36646 CrossRef Medline
15. Greife, A., Felekyan, S., Ma, Q., Gertzen, C. G. W., Spomer, L., Dimura, M., Peulen, T. O., Wöhler, C., Häussinger, D., Gohlke, H., Keitel, V., and Seidel, C. A. (2016) Structural assemblies of the di- and oligomeric G-protein coupled receptor TGR5 in live cells: an MFIS–FRET and integrative modelling study. *Sci. Rep.* **6,** 36792 CrossRef Medline
16. Marcoux, J., Man, P., Petit-Haertlein, I., Vivès, C., Forest, E., and Fieschi, F. (2010) p47^{phox} molecular activation for assembly of the neutrophil NADPH oxidase complex. *J. Biol. Chem.* **285,** 28980–28990 CrossRef Medline
17. Grailhe, R., Merola, F., Ridard, J., Couvignou, S., Le Poupon, C., Changeux, J.-P., and Laguitton-Pasquier, H. (2006) Monitoring protein interactions in the living cell through the fluorescence decays of the cyan fluorescent protein. *ChemPhysChem* **7,** 1442–1454 CrossRef Medline
18. Vogel, S. S., Thaler, C., and Koushik, S. V. (2006) Fanciful FRET. *Sci. STKE* **2006,** re2CrossRef Medline
19. Stasia, M. J., and Li, X. J. (2008) Genetics and immunopathology of chronic granulomatous disease. *Semin. Immunopathol.* **30,** 209–235 CrossRef Medline
20. Nauseef, W. M. (2004) Assembly of the phagocyte NADPH oxidase. *Histochem. Cell Biol.* **122,** 277–291 CrossRef Medline
21. Foo, Y. H., Naredi-Rainer, N., Lamb, D. C., Ahmed, S., and Wohland, T. (2012) Factors affecting the quantification of biomolecular interactions by fluorescence cross-correlation spectroscopy. *Biophys. J.* **102,** 1174–1183 CrossRef Medline
22. Karimi, G., Houée Levin, C., Dagher, M. C., Baciou, L., and Bizouarn, T. (2014) Assembly of phagocyte NADPH oxidase: A concerted binding process? *Biochim. Biophys. Acta* **1840,** 3277–3283 CrossRef Medline
23. Durand, D., Vivès, C., Cannella, D., Pérez, J., Pebay-Peyroula, E., Vachette, P., and Fieschi, F. (2010) NADPH oxidase activator p67^{phox} behaves in solution as a multidomain protein with semi-flexible linkers. *J. Struct. Biol.* **169,** 45–53 CrossRef Medline
24. Durand, D., Cannella, D., Dubosclard, V., Pebay-Peyroula, E., Vachette, P., and Fieschi, F. (2006) Small-angle X-ray scattering reveals an extended organization for the autoinhibitory resting state of the p47^{phox} modular protein. *Biochemistry* **45,** 7185–7193 CrossRef Medline
25. Karathanassis, D., Stahelin, R. V., Bravo, J., Perisic, O., Pacold, C. M., Cho, W., and Williams, R. L. (2002) Binding of the PX domain of p47^{phox} to phosphatidylinositol 3,4-bisphosphate and phosphatidic acid is masked by an intramolecular interaction. *EMBO J.* **21,** 5057–5068 CrossRef Medline
26. Svergun, D., Barberato, C., and Koch, M. H. J. (1995) CRYSOL: a program to evaluate x-ray solution scattering of biological macromolecules from atomic coordinates. *J. Appl. Crystallogr.* **28,** 768–773 CrossRef
27. Wilson, M. I., Gill, D. J., Perisic, O., Quinn, M. T., and Williams, R. L. (2003) PB1 domain-mediated heterodimerization in NADPH oxidase and signaling complexes of atypical protein kinase C with Par6 and p62. *Mol. Cell* **12,** 39–50 CrossRef Medline
28. Yuzawa, S., Miyano, K., Honbou, K., Inagaki, F., and Sumimoto, H. (2009) The domain organization of p67^{phox}, a protein required for activation of the superoxide-producing NADPH oxidase in phagocytes. *J. Innate Immun.* **1,** 543–555 CrossRef Medline
29. Kami, K., Takeya, R., Sumimoto, H., and Kohda, D. (2002) Diverse recognition of non-PxxP peptide ligands by the SH3 domains from p67^{phox}, Grb2 and Pex13p. *EMBO J.* **21,** 4268–4276 CrossRef Medline
30. Cifuentes-Pagano, M. E., Meijles, D. N., and Pagano, P. J. (2015) Nox inhibitors & therapies: rational design of peptidic and small molecule inhibitors. *Curr. Pharm. Design* **21,** 6023–6035
31. Laraia, L., McKenzie, G., Spring, D. R., Venkitaraman, A. R., and Huggins, D. J. (2015) Overcoming chemical, biological, and computational challenges in the development of inhibitors targeting protein–protein interactions. *Chem. Biol.* **22,** 689–703 CrossRef Medline
32. DeLeo, F. R., and Quinn, M. T. (1996) Assembly of the phagocyte NADPH oxidase: molecular interaction of oxidase proteins. *J. Leukoc. Biol.* **60,** 677–691 CrossRef Medline
33. Boura, E., Rózycki, B., Herrick, D. Z., Chung, H. S., Vecer, J., Eaton, W. A., Cafiso, D. S., Hummer, G., and Hurley, J. H. (2011) Solution structure of the ESCRT-I complex by small-angle X-ray scattering, EPR, and FRET spectroscopy. *Proc. Natl. Acad. Sci. U.S.A.* **108,** 9437–9442 CrossRef Medline
34. Fuertes, G., Banterle, N., Ruff, K. M., Chowdhury, A., Mercadante, D., Koehler, C., Kachala, M., Estrada Girona, G., Milles, S., Mishra, A., Onck,

P. R., Gräter, F., Esteban-Martín, S., Pappu, R. V., Svergun, D. I., *et al.* (2017) Decoupling of size and shape fluctuations in heteropolymeric sequences reconciles discrepancies in SAXS vs. FRET measurements. *Proc. Natl. Acad. Sci. U.S.A.* **114,** E6342–E6351 CrossRef Medline

35. Peti, W., Page, R., Boura, E., and Rózycki, B. (2018) Structures of dynamic protein complexes: hybrid techniques to study MAP kinase complexes and the ESCRT system. *Methods Mol. Biol.* **1688,** 375–389 CrossRef Medline
36. Faure, M. C., Sulpice, J.-C., Delattre, M., Lavielle, M., Prigent, M., Cuif, M.-H., Melchior, C., Tschirhart, E., Nüsse, O., and Dupré-Crochet, S. (2013) The recruitment of $p47^{phox}$ and Rac2G12V at the phagosome is transient and phosphatidylserine dependent. *Biol. Cell* **105,** 501–518 CrossRef Medline
37. Song, Z. M., Bouchab, L., Hudik, E., Le Bars, R., Nüsse, O., and Dupré-Crochet, S. (2017) Phosphoinositol 3-phosphate acts as a timer for reactive oxygen species production in the phagosome. *J. Leukoc. Biol.* **101,** 1155–1168 CrossRef Medline
38. Lapouge, K., Smith, S. J., Walker, P. A., Gamblin, S. J., Smerdon, S. J., and Rittinger, K. (2000) Structure of the TPR domain of $p67^{phox}$ in complex with Rac·GTP. *Mol. Cell* **6,** 899–907 CrossRef Medline
39. Goedhart, J., van Weeren, L., Hink, M. A., Vischer, N. O., Jalink, K., and Gadella, T. W., Jr. (2010) Bright cyan fluorescent protein variants identified by fluorescence lifetime screening. *Nat. Methods* **7,** 137–139 CrossRef Medline
40. Erard, M., Fredj, A., Pasquier, H., Beltolngar, D. B., Bousmah, Y., Derrien, V., Vincent, P., and Merola, F. (2013) Minimum set of mutations needed to optimize cyan fluorescent proteins for live cell imaging. *Mol. Biosyst.* **9,** 258–267 CrossRef Medline
41. Herbomel, G., Hatte, G., Roul, J., Padilla-Parra, S., Tassan, J. P., and Tramier, M. (2017) Actomyosin-generated tension on cadherin is similar between dividing and non-dividing epithelial cells in early *Xenopus laevis* embryos. *Sci. Rep.* **7,** 45058 CrossRef Medline
42. Demeautis, C., Sipieter, F., Roul, J., Chapuis, C., Padilla-Parra, S., Riquet, F. B., and Tramier, M. (2017) Multiplexing PKA and ERK1&2 kinases FRET biosensors in living cells using single excitation wavelength dual colour FLIM. *Sci. Rep.* **7,** 41026 CrossRef Medline
43. Poëa-Guyon, S., Pasquier, H., Mérola, F., Morel, N., and Erard, M. (2013) The enhanced cyan fluorescent protein: a sensitive pH sensor for fluorescence lifetime imaging. *Anal. Bioanal. Chem.* **405,** 3983–3987 CrossRef Medline
44. Zachariassen, L. G., Katchan, L., Jensen, A. G., Pickering, D. S., Plested, A. J., and Kristensen, A. S. (2016) Structural rearrangement of the intracellular domains during AMPA receptor activation. *Proc. Natl. Acad. Sci. U.S.A.* **113,** E3950–E3959 CrossRef Medline
45. Valeur, B. (2006) *Molecular Fluorescence: Principles and Applications*, 3rd Ed., Wiley-VCH, Weinheim, Germany
46. Espagne, A., Erard, M., Madiona, K., Derrien, V., Jonasson, G., Lévy, B., Pasquier, H., Melki, R., and Mérola, F. (2011) Cyan fluorescent protein carries a constitutive mutation that prevents its dimerization. *Biochemistry* **50,** 437–439 CrossRef Medline
47. Heikal, A. A., Hess, S. T., Baird, G. S., Tsien, R. Y., and Webb, W. W. (2000) Molecular spectroscopy and dynamics of intrinsically fluorescent proteins: coral red (dsRed) and yellow (Citrine). *Proc. Natl. Acad. Sci. U.S.A.* **97,** 11996–12001 CrossRef Medline
48. Vogel, S. S., van der Meer, B. W., and Blank, P. S. (2014) Estimating the distance separating fluorescent protein FRET pairs. *Methods* **66,** 131–138 CrossRef Medline
49. Steinberg, I. Z. (1968) Nonradiative energy transfer in systems in wich rotatory brownian motion is frozen. *J. Chem. Phys.* **48,** 2411 CrossRef
50. Kenworthy, A. K., and Edidin, M. (1998) Distribution of a glycosylphosphatidylinositol-anchored protein at the apical surface of MDCK cells examined at a resolution of <100 Å using imaging fluorescence resonance energy transfer. *J. Cell Biol.* **142,** 69–84 CrossRef Medline
51. Kenworthy, A. K., Petranova, N., and Edidin, M. (2000) High-resolution FRET microscopy of cholera toxin B-subunit and GPI-anchored proteins in cell plasma membranes. *Mol. Biol. Cell* **11,** 1645–1655 CrossRef Medline
52. Zacharias, D. A., Violin, J. D., Newton, A. C., and Tsien, R. Y. (2002) Partitioning of lipid-modified monomeric GFPs into membrane microdomains of live cells. *Science* **296,** 913–916 CrossRef Medline
53. Kofoed, E. M., Guerbadot, M., and Schaufele, F. (2010) Structure, affinity, and availability of estrogen receptor complexes in the cellular environment. *J. Biol. Chem.* **285,** 2428–2437 CrossRef Medline
54. Bohmer, M., Wahl, M., Rahn, H. J., Erdmann, R., and Enderlein, J. (2002) Time-resolved fluorescence correlation spectroscopy. *Chem. Phys. Lett.* **353,** 439–445 CrossRef
55. Padilla-Parra, S., Audugé, N., Coppey-Moisan, M., and Tramier, M. (2011) Dual-color fluorescence lifetime correlation spectroscopy to quantify protein–protein interactions in live cell. *Microsc. Res. Techniq.* **74,** 788–793 CrossRef
56. Padilla-Parra, S., Audugé, N., Coppey-Moisan, M., and Tramier, M. (2014) Quantitative study of protein-protein interactions in live cell by dual-color fluorescence correlation spectroscopy. *Methods Mol. Biol.* **1076,** 683–698 CrossRef Medline
57. Konarev, P. V., Volkov, V. V., Sokolova, A. V., Koch, M. H. J., and Svergun, D. I. (2003) PRIMUS: a Windows PC-based system for small-angle scattering data analysis. *J. Appl. Crystallogr.* **36,** 1277–1282 CrossRef
58. Petoukhov, M. V., and Svergun, D. I. (2005) Global rigid body modeling of macromolecular complexes against small-angle scattering data. *Biophys. J.* **89,** 1237–1250 CrossRef Medline
59. Moore, B. L., Kelley, L. A., Barber, J., Murray, J. W., and MacDonald, J. T. (2013) High-quality protein backbone reconstruction from alpha carbons using gaussian mixture models. *J. Comput. Chem.* **34,** 1881–1889 CrossRef Medline
60. Krivov, G. G., Shapovalov, M. V., and Dunbrack, R. L., Jr. (2009) Improved prediction of protein side-chain conformations with SCWRL4. *Proteins* **77,** 778–795 CrossRef Medline
61. Tria, G., Mertens, H. D., Kachala, M., and Svergun, D. I. (2015) Advanced ensemble modelling of flexible macromolecules using X-ray solution scattering. *IUCrJ* **2,** 207–217 CrossRef Medline
62. Valentini, E., Kikhney, A. G., Previtali, G., Jeffries, C. M., and Svergun, D. I. (2015) SASBDB, a repository for biological small-angle scattering data. *Nucleic Acids Res.* **43,** D357–D363 CrossRef Medline